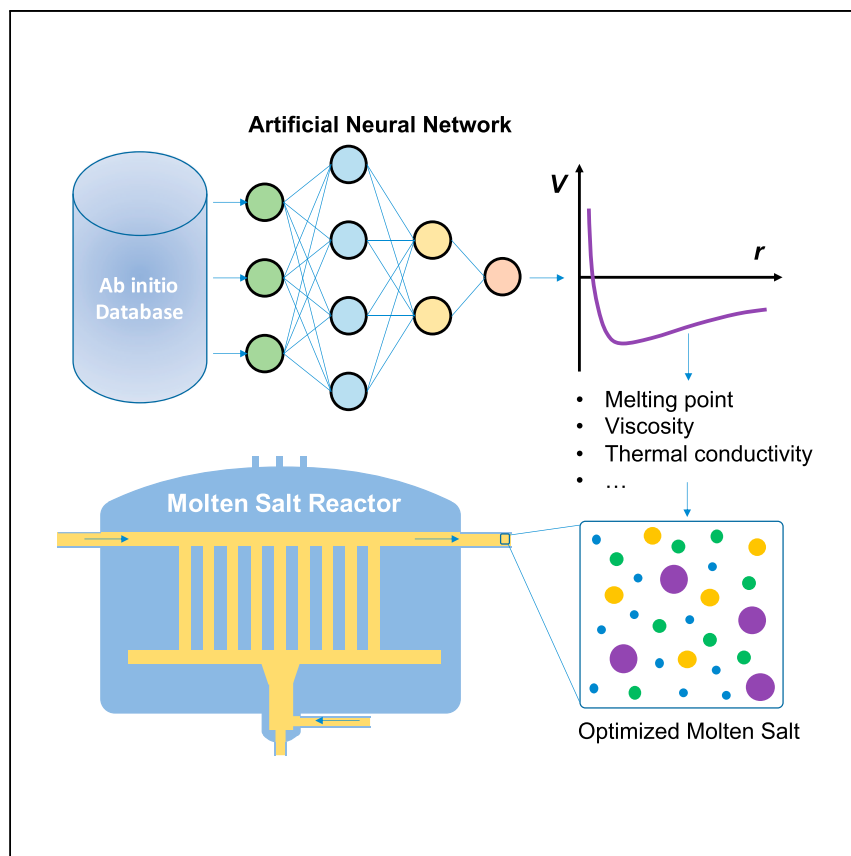


Article

# Development of robust neural-network interatomic potential for molten salt



Molten salts are an important medium for heat storage/transfer in clean energy applications, such as nuclear and solar energy, yet atomistic-level modeling of the thermophysical properties of molten salts remains a challenge. Li et al. demonstrate the robustness of neural network interatomic potential for accurate and efficient molten salt modeling.

Qing-Jie Li, Emine Küçükbenli, Stephen Lam, Boris Khaykovich, Efthimios Kaxiras, Ju Li

bkh@mit.edu (B.K.)  
liju@mit.edu (J.L.)

## HIGHLIGHTS

Fundamental considerations in molten salt modeling with artificial neural network (NN)

Medium-ranged NN interatomic potentials (NNIPs) suffice to describe ionic liquids

NNIP achieves near first-principles accuracy yet is  $\sim 10^3 \times$  efficient

NNIP accurately predicts a wide range of thermophysical properties of molten salts

Article

# Development of robust neural-network interatomic potential for molten salt

Qing-Jie Li,<sup>1,8</sup> Emine Küçükbenli,<sup>2,3,8</sup> Stephen Lam,<sup>1,4</sup> Boris Khaykovich,<sup>5,\*</sup> Efthimios Kaxiras,<sup>2,6</sup> and Ju Li<sup>1,7,9,\*</sup>

## SUMMARY

Molten salts are a promising class of ionic liquids for clean energy applications, such as nuclear and solar energy. However, efficient and accurate evaluation of salt properties from a fundamental, microscopic perspective remains a challenge. Here, we apply artificial neural networks to atomistic modeling of molten NaCl to accurately reproduce the properties from *ab initio* quantum mechanical calculations based on density functional theory (DFT). The obtained neural network interatomic potential (NNIP) effectively captures the effects of both long-range and short-range interactions, which are crucial for modeling ionic liquids. Extensive validations suggest that the NNIP is capable of predicting the structural, thermophysical, and transport properties of molten NaCl as well as properties of crystalline NaCl, demonstrating near-DFT accuracy and  $10^3\times$  higher efficiency in atomistic simulations. This application of NNIP suggests a paradigm shift from empirical/semiempirical/*ab initio* approaches to an efficient and accurate machine learning scheme in molten salt modeling.

## INTRODUCTION

Molten salts have been widely exploited for clean energy applications, such as molten salt reactors (MSRs)<sup>1-3</sup> and concentrated solar power (CSP) technologies.<sup>4,5</sup> A major role played by molten salts in these applications is to transfer/store heat that can be subsequently converted into other energy forms. Safe and efficient heat transfer and storage require excellent thermophysical and transport properties of clean salts (e.g., melting point, heat capacity, thermal conductivity, viscosity, vapor pressure, diffusivity, etc.).<sup>2</sup> Moreover, practical concerns, such as stability under extreme conditions,<sup>6</sup> tolerance to impurities,<sup>7</sup> and compatibility with major structural materials,<sup>8</sup> need to be addressed. Due to the high-dimensional nature of materials space, searching for appropriate salt systems and their optimization for various applications remain essential challenges, requiring a deep understanding of the underlying molecular structures, chemistry, and dynamics of relevant molten salts.

Expediting the discovery of the desired salt system hidden in a vast materials space generally requires:

- (1) efficient searching algorithms, such as Bayesian optimization,<sup>9,10</sup> to balance exploration and exploitation and
- (2) fast yet accurate evaluation of a new system in the high-dimensional space.

<sup>1</sup>Department of Nuclear Science and Engineering, Massachusetts Institute of Technology, Cambridge, MA 02139, USA

<sup>2</sup>Department of Physics and School of Engineering and Applied Sciences, Harvard University, Cambridge, MA 02138, USA

<sup>3</sup>Department of Information Systems, Questrom School of Business, Boston University, Boston, MA 02215, USA

<sup>4</sup>Department of Chemical Engineering, University of Massachusetts Lowell, Lowell, MA 01854, USA

<sup>5</sup>Nuclear Reactor Laboratory, Massachusetts Institute of Technology, Cambridge, MA 02139, USA

<sup>6</sup>Department of Physics, Harvard University, Cambridge, MA 02138, USA

<sup>7</sup>Department of Materials Science and Engineering, Massachusetts Institute of Technology, Cambridge, MA 02139, USA

<sup>8</sup>These authors contributed equally

<sup>9</sup>Lead contact

\*Correspondence: [bkh@mit.edu](mailto:bkh@mit.edu) (B.K.), [lju@mit.edu](mailto:lju@mit.edu) (J.L.)

<https://doi.org/10.1016/j.xcrp.2021.100359>

Very often, the latter requirement constitutes the rate-limiting step. For example, experimental techniques, such as neutron and X-ray diffraction and electrochemical measurements,<sup>11-17</sup> are generally expensive and challenging under extreme conditions and stringent impurity control. *Ab initio* molecular dynamics (AIMD) simulations, such as those based on density functional theory (DFT),<sup>18,19</sup> have been successful in modeling various molten salts,<sup>20-28</sup> but this is costly for properties (e.g., melting temperature, heat capacity, thermal conductivity, etc.) that require statistics on relatively large time and length scales. Classical atomistic simulations based on physics-informed empirical interatomic potentials<sup>29-33</sup> are many orders of magnitude faster than AIMD, but their accuracy is generally limited by the expressive power of the functional form employed for the potential. Evaluating properties in molten salts space, both experimentally and computationally, is subjected to an accuracy-versus-cost trade-off. Machine-learning-based interatomic potentials (MLIPs)<sup>34-41</sup> are emerging as a promising solution to alleviate this problem. Specifically, MLIPs have been shown to afford accuracy close to that of DFT calculations at a computational cost comparable to (although typically higher than) that of classical empirical interatomic potentials. MLIPs empower accurate and efficient MD simulations with  $10^3$ – $10^4$  atoms on the timescale of nanoseconds, offering unprecedented opportunities to explore molten salt space.

In this work, we choose NaCl as a prototype system to demonstrate the feasibility of applying an artificial neural-network (NN) framework in training high-quality interatomic potentials for modeling molten salts. We emphasize that the effects of long-range Coulombic interactions and short-range repulsive interactions, both of which are crucial in modeling ionic liquids with high-temperature dynamics, can be effectively captured by a medium-ranged NN interatomic potential (NNIP). This has been achieved by a carefully designed, balanced training dataset. Extensive evaluations suggest that our NNIP is capable of predicting the structural, thermo-physical, and transport properties of molten NaCl as well as common crystal properties, with an accuracy close to AIMD simulations. Furthermore, most of our NNIP predictions are also in good agreement with experimental measurements, suggesting NNIP as a robust approach for accurate and efficient modeling of molten salts.

## RESULTS

### Artificial NN framework

To model the high-dimensional potential energy surface of molten NaCl with a large number of atoms, we follow the framework of Behler and Parrinello<sup>34</sup> to represent the total potential energy of a system as a sum of atomic contributions,

$$E = \sum_i^{N_{\text{at}}} E_i(G_i), \quad (\text{Equation 1})$$

where a species-specific fully connected NN takes the local atomic environment descriptor  $G_i$  of a single atom  $i$  as input and outputs the atomic contribution  $E_i$  to the total energy;  $N_{\text{at}}$  is the total number of atoms in the system. In this work, both Na and Cl share the same atomic NN architecture but with different optimized weights and biases. A few hidden layers can be used for a higher level abstraction of the input information. We used two hidden layers in the current work. See [Figure S1](#) for more details.

The local atomic environment of a given atom  $i$  is described by a vector that is built from Behler-Parinello symmetry functions,<sup>34</sup> with modifications proposed by Smith et al.<sup>37</sup> and Lot et al.<sup>42</sup> These functions include two-body (radial) and three-body

(angular) descriptors that specify a local atomic environment in a species-resolved manner. The radial descriptor is defined as

$$G_i^R[s] = \sum_{j \neq i}^{N_p} e^{-\eta(R_{ij}-R_s)^2} f_c(R_{ij}), \quad (\text{Equation 2})$$

where  $\eta$  and a set of Gaussian centers  $R_s$  are parameters of the descriptor defined by the user. The sum runs over all pairs  $N_p$  between atoms of a given species, whose distance  $R_{ij}$  from the central atom is within a cutoff distance  $R_c$ . The cutoff function that smoothly diminishes beyond the cutoff distance is defined as

$$f_c(R_{ij}) = \left[ 0.5 \cos\left(\frac{\pi R_{ij}}{R_c}\right) + 0.5 \right] \text{ for } R_{ij} \leq R_c; 0.0 \text{ for } R_{ij} > R_c. \quad (\text{Equation 3})$$

The angular descriptor is defined as

$$G_i^A[s] = 2^{1-\zeta} \sum_{j,k \neq i}^{N_t} (1 + \cos(\theta_{ijk} - \theta_s))^\zeta e^{-\eta\left(\frac{R_{ij}+R_{ik}}{2}-R_s\right)^2} f_c(R_{ij})f_c(R_{ik}), \quad (\text{Equation 4})$$

where the sum runs over all pairs  $N_t$  of neighboring atoms  $j$  and  $k$  for a given species triplet, with interatomic distances of  $R_{ij}$  and  $R_{ik}$  within the cutoff radius, and forming an angle  $\theta_{ijk}$  with it. The parameters  $\eta$  and  $\zeta$  control the width of the Gaussian and cosine functions, although the sets of  $R_s$  and  $\theta_s$  determine the peak positions. Together, these user-defined parameters determine the radial and angular resolution of the descriptor and are tuned to achieve sufficient resolution. See the section [Experimental procedures](#) for more details.

### Ab initio dataset

The design of a robust NNIP depends crucially on the choice of training dataset. For molten salt applications, the primary focus is on liquid properties, such as the melting point ( $T_m$ ), heat capacity ( $C_p$ ), thermal conductivity ( $\lambda$ ), diffusion coefficient ( $D$ ), density ( $\rho$ ), molecular structure, equation of state, etc. For robustness, the NNIP should also be able to make reasonably good predictions on common crystal properties. To this end, we constructed our training dataset using an iterative augmentation procedure based on quick training-validation-augmentation cycles. This procedure, similar to active learning, allows us to efficiently identify the configurations where NNIP predictions are far from DFT results. By adding these relevant configurations to the training set and retraining the NN, we build a more robust NNIP at each cycle. The constitution of the final training dataset is shown in [Figure S2](#). Specifically, our training dataset includes normal liquid (disordered) configurations from zero-pressure MD trajectories ( $T = 900$  K, 1,000 K, 1,100 K, 1,200 K, and 1,300 K and quenching from 3,000 K to 1,100 K), compressed liquid (some are partially crystallized) configurations up to  $\sim 10$  GPa (from  $T = 1,100$  K to  $T = 1,300$  K), high-temperature liquid ( $T = 5,000$  K, 10,000 K, and 20,000 K) under a confined volume, non-1:1 Na/Cl ratio liquid ( $T = 1,100$  K, 1,200 K, and 1,300 K), high-temperature crystals (near the melting point,  $T = 900$  K and 1,000 K), zero-temperature crystal (subjected to hydrostatic pressures, shear, and uniaxial deformation), dimer configurations (Na-Na, Na-Cl, and Cl<sup>-</sup>-Cl from  $\sim 1$  to 8 Å) in the gas phase, and two isolated Na and Cl atoms. The number of total configurations in our training dataset is  $\sim 112,000$  (see [Table S1](#) for more details). We note that adding compressed liquids, high-temperature liquids, and short-range dimer configurations can help stabilize dynamics and prevent non-physical clustering at short ranges (where the NN hardly learns because of less available data). Similarly, non-1:1 Na/Cl ratio liquid configurations are important to balance local environments showing compositional

fluctuations. As will be demonstrated shortly, such a composition of training dataset leads to excellent training and testing results for both liquid and crystalline NaCl properties.

### NNIP predictions on energy, forces, and dynamics

We test our NNIP potential in three steps that cover a wide range of use scenarios.

- (1) We assess the prediction performance by using the 20% of the dataset that is separated for testing, which consists of configurations that are similar to the ones of the training set (basic testing).
- (2) We test the ability of the potential to generate a stable MD trajectory (interpolation testing). We make this scenario more challenging by simulating a microcanonical ensemble ( $NVE$ , constant number of atoms  $N$ , volume  $V$ , and total energy  $E$ ), without the use of a thermostat, so that the error due to wrong predictions would accumulate to divert the system from constant total energy dynamics.
- (3) We assess the prediction quality of NNIP on configurations that are less correlated to the ones in the training dataset and/or on the prediction of properties that are not utilized during the training of the NNIP (extrapolation testing), such as radial distribution function, equation of state, and density. Finally, we use our NNIP to explore properties that are beyond affordable *ab initio* simulations, such as heat capacity, thermal conductivity, diffusion coefficient, and melting temperature, as well as elastic properties of crystalline phases and surfaces and compare its predictions with experimental observations.

We first report the basic testing errors of our final NNIP model. As the current NNIP is mainly developed for simulating molten NaCl, the testing errors are based on evaluating unseen configurations from normal MD trajectories, such as liquid (disordered) structures from 900 K to 1,300 K as well as crystalline structures near the melting point. In total, there are  $\sim 18,400$  structures in the test dataset. In [Figure 1](#), the deviation of NNIP predictions from DFT results for potential energy and atomic forces is reported. The testing errors in both potential energy and atomic forces largely follow a Gaussian distribution (see the histogram plot and normal distribution fitting on the right side of [Figures 1A](#) and [1B](#)); thus, we use root mean square error (RMSE) as a measure of the overall testing errors. Specifically, the RMSE of total potential energy predictions reaches a value as low as 1.52 meV/atom, although the RMSE of atomic forces predictions is 0.04 eV/Å. Such small testing errors suggest an accuracy close to DFT level. The two distinct clusters in [Figure 1A](#) are due to the potential energy differences between crystalline structures and liquid/disordered structures. When the testing dataset includes all configurations with the same proportions as shown in [Figure S2](#), that is, the full validation set that corresponds to 20% of the total dataset, then the RMSEs of total energy predictions and atomic force predictions become 7.9 meV/atom and 0.07 eV/Å, respectively, still quite accurate, considering that the distribution has longer tail (larger kurtosis) than a Gaussian and overestimates the average spread (see [Figure S3](#)).

A good interatomic potential should exhibit smoothness in atomic forces as a function of continuously changing atomic positions. This capability of interpolation between learned snapshots of configurations is particularly important in actual MD simulations, where stability of the dynamics is required to continuously sample the configurational space. To assess this capability, we carry out the challenging test of energy conservation during microcanonical ensemble; that is, we test whether the NNIP forces are smooth enough to allow high-accuracy time integration so that total energy is conserved during

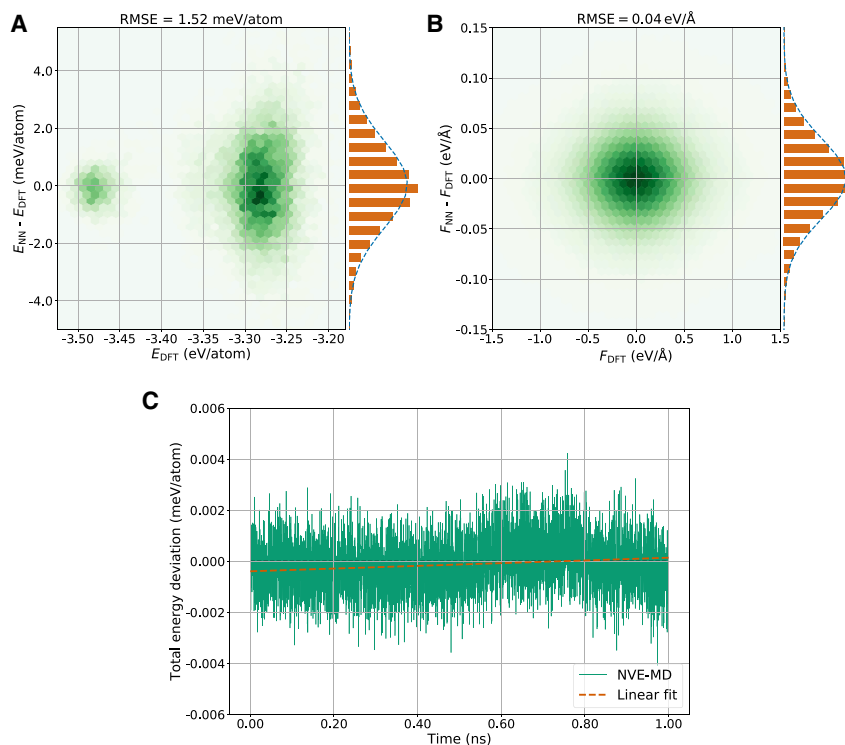


**Figure 1. Basic testing and interpolation testing of NNIP**

(A) Testing errors in total potential energies.

(B) Testing errors in atomic forces. The distribution of both testing errors largely follows a Gaussian distribution, as shown in the histogram plot and corresponding normal distribution fitting. Color intensities of 2D bins indicates the counts of data points. As the NNIP is mainly targeted for MD simulations on molten NaCl, testing errors are reported based on unseen configurations from normal MD trajectories, such as liquid (disordered) structures from 900 K to 1,300 K and crystalline structures near the melting point.

(C) Conservation of total energy in an NVE MD simulation. The MD simulation was performed at  $T = 1,530$  K at a time step of 1 fs. The total energy drift within 1 ns is on the order of  $10^{-3}$  meV/atom, suggesting excellent stability of high-temperature dynamics.

a simulation. Specifically, in a properly integrated (at a time step of 1 fs) NVE MD simulation without any thermostats, good atomic force predictions should in principle conserve the total energy, although poor or noisy force predictions may lead to spurious atomic velocities, breaking energy conservation. Note that smoothness of the predicted potential energy surface and conservation of the total energy is not a sufficient condition but a necessary condition of an accurate NNIP model. We performed MD simulations under NVE ensemble with 1,728 atoms at  $\sim 1,530$  K (well above the melting point, thus high-temperature dynamics), with a time step of 1 fs. As seen in Figure 1C, on the timescale of 1 ns, the total energy drift during this simulation is only on the order of  $10^{-3}$  meV/atom, demonstrating excellent stability of high-temperature dynamics. These evaluations on both the discrete configurations in the testing dataset and dynamic MD trajectories at high temperature thus suggest that the current NNIP is capable of simulating molten NaCl with energy/force predictions on DFT-level accuracy.

### NNIP predictions on the liquid-phase atomic structures

Next, we test our NNIP in terms of various liquid properties that are often considered when identifying candidate molten salts. We first examine the liquid structures from both our AIMD simulations and NNIP-MD simulations. To effectively describe the average structure

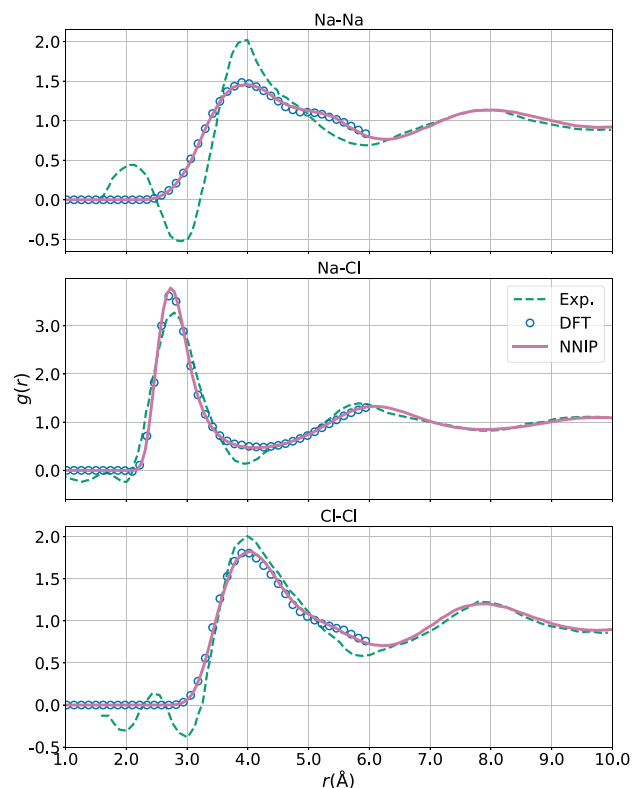


**Figure 2. Radial distribution functions (RDFs) of liquid NaCl at 1,150 K**

All three partial RDFs predicted by NNIP-MD using a 512-atom supercell excellently match those from AIMD. Both AIMD and NNIP-MD were performed under *NVT* ensemble at  $T = 1,150$  K. The equilibrium supercell lengths for AIMD and NNIP-MD are 12.38 Å and 24.91 Å, respectively. Experimental measurements were adopted from Edwards et al.<sup>14</sup> and Biggin and Enderby.<sup>15</sup>

of liquid NaCl, we computed partial radial distribution functions (RDFs) for all three atomic-pairs (Na-Na, Na-Cl, and Cl<sup>-</sup>-Cl). Specifically, we carried out both AIMD and NNIP-MD simulations under the same conditions, such as *NVT* ensemble (constant number of atoms  $N$ , volume  $V$ , and temperature  $T$ ) with  $T = 1,150$  K and at equilibrium volume. After 10 ps equilibration, average RDFs were computed from MD trajectories over 66 ps and 90 ps for AIMD and NNIP-MD, respectively. As shown in Figure 2, partial RDFs from NNIP-MD simulation (black solid line) almost overlap with those from AIMD simulation (yellow circles with shaded bands indicating the standard deviations), and both AIMD and NNIP-MD show the same first and second peak positions ( $R_1^{\text{NaNa}} = 3.9$  Å,  $R_1^{\text{NaCl}} = 2.7$  Å,  $R_1^{\text{ClCl}} = 4.0$  Å,  $R_2^{\text{NaNa}} = 8.1$  Å,  $R_2^{\text{NaCl}} = 6.2$  Å,  $R_2^{\text{ClCl}} = 8.0$  Å) and overlapping shoulders after the first peak in both Na-Na and Cl-Cl RDFs, thus suggesting excellent agreement between NNIP-MD and AIMD. Partial RDFs can also be deduced from neutron diffraction measurement using isotopic substitution method;<sup>14,15</sup> the only published measurement for molten NaCl ( $T = 1,148$  K) was made in the 1970s<sup>14</sup> and was later corrected with updated neutron scattering amplitudes for Cl isotopes.<sup>15</sup> As seen in Figure 2, both AIMD and NNIP-MD are consistent with experimental measurements in the first and second peak positions and the profile after the first minimum; however, some deviations in peak amplitude and shape appear below the first minimum. Such deviations have also been observed in a previous DFT study using various exchange-correlation density functionals (see Figure S4 for a comparison between different AIMD simulations).<sup>43</sup> The short-range RDFs in experimental measurements may be limited by a small  $Q$  cutoff (1.5–12 Å<sup>-1</sup>),<sup>14</sup> which points to the need for better measurements with higher  $Q$  cutoff and higher  $Q$  resolution.

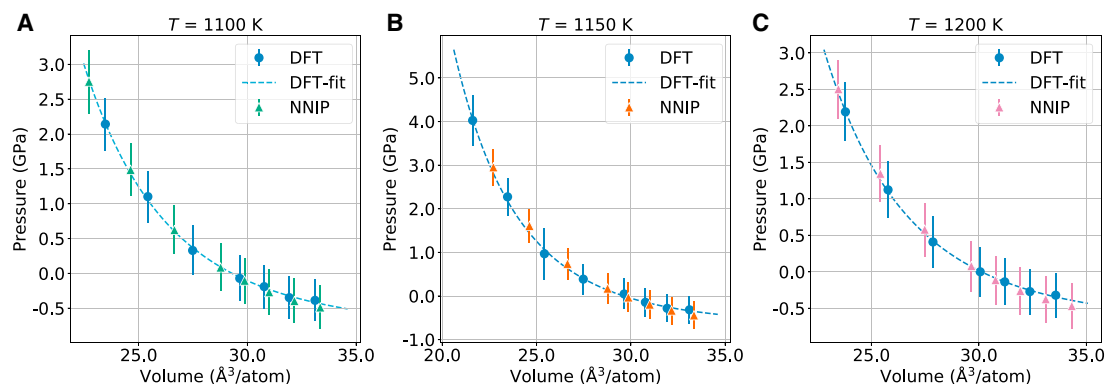


**Figure 3. Equations of state**

Equation of state (EOS) at (A) 1,100 K, (B) 1,150 K, and (C) 1,200 K. All NNIP-MD simulations were performed for 1 ns, and each data point was averaged over the last 0.9 ns. AIMD simulations were carried out for 40 ps, and each data point was averaged over the last 36 ps. Error bars correspond to standard deviations.

### NNIP predictions on the equation of state

The equation of state (EOS) is another important metric for testing relations between thermodynamic state variables. Figure 3 shows the relationship between pressure  $P$  and the average atomic volume  $V$  at three temperatures. As can be seen from this figure, the NNIP-MD results are in excellent agreement with AIMD in the pressure range 3.0 GPa to  $-0.5$  GPa. Note that deviations at negative pressure range are slightly larger than those in the positive pressure range. This is because configurations under negative pressures were not included in our training dataset. By fitting both AIMD and NNIP-MD data to the Murnaghan equation of state,

$$P(V) = \frac{B}{B'} \left[ \left( \frac{V}{V_0} \right)^{-B'} - 1 \right], \quad (\text{Equation 5})$$

we can further compare the bulk modulus  $B$  ( $B'$  is the first derivative of  $B$  with respect to pressure) and equilibrium volume  $V_0$ . For the three temperatures considered here, the bulk moduli from AIMD simulations are 4.8 GPa, 4.2 GPa, and 4.3 GPa, although the NNIP predictions are 5.3 GPa, 5.1 GPa, and 5.0 GPa, with increasing temperature, respectively. On average, the NNIP predicted bulk moduli are  $\sim 15\%$  higher than that from AIMD. Such generally higher bulk modulus should be due to the slight deviations in the negative pressure range, which increases the slope of Equation 5. Nevertheless, the NNIP-predicted equilibrium volumes at the three temperatures are 29.3, 29.6, and 30.1 (in units of  $\text{\AA}^3/\text{atom}$ ), in excellent agreement with the AIMD results 29.3, 29.7, and 30.1, respectively. From these equilibrium volumes at three closely spaced temperature values, we can further estimate the volumetric thermal expansion coefficient,

$$\alpha_V = \frac{1}{V} \left( \frac{\partial V}{\partial T} \right)_P. \quad (\text{Equation 6})$$

Both NNIP and AIMD predict a volumetric thermal expansion coefficient of  $2.7 \times 10^{-4} \text{ K}^{-1}$  for  $T = 1,150 \text{ K}$ , close to the experimentally measured<sup>44</sup>  $\alpha_V$  of  $3.1 \times 10^{-4} \text{ K}^{-1}$ .

Following the above discussion on the thermal expansion coefficient, we further compare mass densities at various temperatures. To efficiently reach equilibrium volumes at different temperatures, all AIMD (64 atoms for 120 ps), NNIP-MD (1,728 atoms for 200 ps), and Fumi-Tosi MD (1,728 atoms for 200 ps) simulations were performed under  $NPT$  ensemble (constant number of atoms  $N$ , pressure  $P$ ,

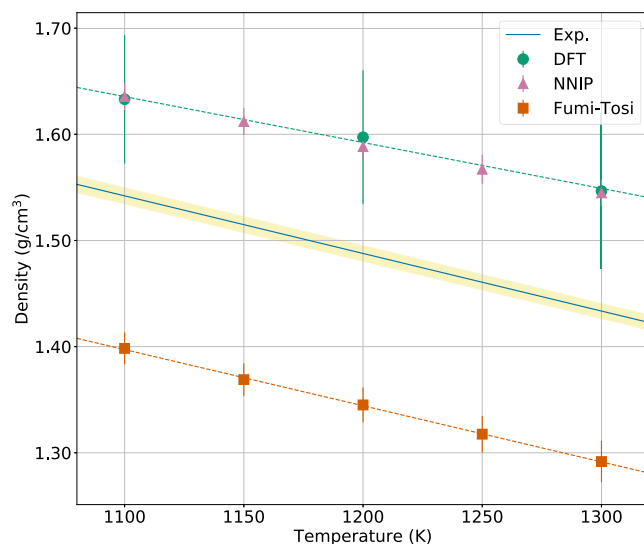


**Figure 4. The mass density of molten NaCl at different temperatures**

NNIP predictions agree very well with AIMD results. Compared to experimental measurement,<sup>45</sup> both NNIP and DFT overestimate the mass densities by ~7% although Fumi-Tosi potential<sup>29</sup> underestimates the mass density by ~10%. Error bars correspond to standard deviations.

and temperature  $T$ ), and the mass densities were averaged over the last 100 ps for each temperature. As shown in Figure 4, over a wide range of temperatures (1,100 K–1,300 K), NNIP once again shows exceptionally good agreement with AIMD. In comparison to experimental measurement,<sup>45</sup> both AIMD and NNIP slightly overestimate the mass densities by ~7%, although the Fumi-Tosi potential underestimates the mass density by ~10%. It should be noted that, because NNIP prediction using 1,728 atoms is in excellent consistency with AIMD results using 64 atoms, the density deviations are unlikely due to finite size effects. Although fluctuations in small-cell simulations are generally large, the time-averaged density over a long simulation is expected to converge to that of large-cell simulations. This has been independently demonstrated using the Fumi-Tosi potential (see Figure S5).<sup>29</sup> We believe the density deviations of AIMD simulations from experimental measurements could be attributed to the approximations involved in DFT calculations, such as electronic exchange-correlation functional and dispersion corrections. It has been highlighted in several previous works<sup>23,43</sup> that the dispersion interaction shows a significant effect on calculated density.

### NNIP predictions on heat capacity

The excellent heat transfer performance of molten salts plays an essential role in both MSR and CSP applications. Among others, heat capacity, self-diffusion coefficient (or viscosity), and thermal conductivity are the most relevant properties controlling heat transfer performance of liquid coolants and heat storage medium. We first compare our NNIP predictions on heat capacity under constant pressure ( $C_p$ ) with experimental measurement and the predictions from the Fumi-Tosi potential.<sup>29</sup> To this end, independent MD simulations (with 4,096 atoms) under  $NPT$  ensemble were carried out in the temperature range from 1,070 K to 1,510 K at zero pressure. The average enthalpy  $H$  at each temperature was then calculated over 100 ps, and the constant pressure heat capacity was evaluated according to

$$C_p = \left( \frac{\partial H}{\partial T} \right)_P. \quad (\text{Equation 7})$$

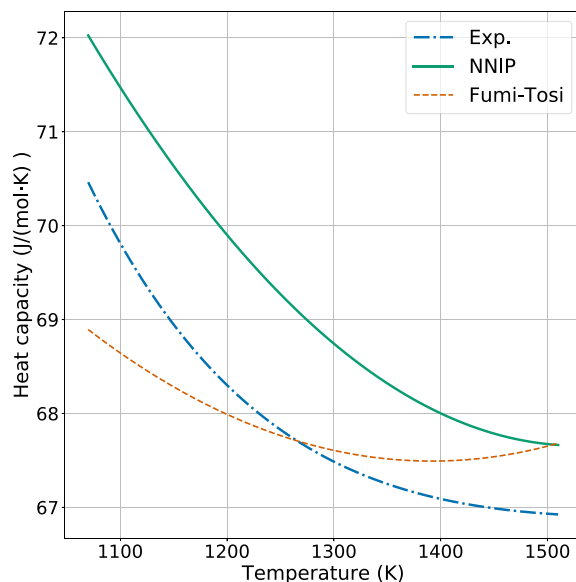


**Figure 5. Heat capacity of molten NaCl over the temperature range from 1,070 K to 1,510 K**  
Heat capacity was calculated from the polynomial fit to the temperature-dependent enthalpy (see Figure S6). A 100-ps-long MD simulation was carried out at each sampled temperature. The largest difference between NNIP predictions from third-order polynomial fitting and experimental measurements is  $\sim 2\%$ . NNIP also predicts a consistent temperature dependence of  $C_p$  with experimental measurement.

Figure 5 shows both the calculated and experimental  $C_p$ . The change of  $H$  with respect to  $T$  was calculated from a third-order polynomial fit to all  $H$ - $T$  data points (see Figure S6). As can be seen, our NNIP-predicted  $C_p$  is overall in good agreement with experimental measurements (blue line),<sup>46</sup> and the largest deviation is  $\sim 2\%$ . Furthermore, the temperature dependence of  $C_p$  from NNIP prediction is in excellent agreement with experimental results. In contrast, although the predictions from the Fumi-Tosi potential<sup>29</sup> show smaller errors at certain temperatures, the predicted temperature dependence significantly deviates from the experimental measurement.

### NNIP predictions on self-diffusion coefficients

The self-diffusion coefficient was calculated by evaluating the slope of mean square displacement (MSD) with respect to time. Due to high computational cost, especially for AIMD simulations, the MSD was determined by multiple-time-origin averaging.<sup>20</sup> All AIMD, NNIP-MD, and Fumi-Tosi MD simulations were carried out under the  $NVT$  ensemble for  $\sim 180$  ps. Figure 6 shows the diffusion coefficients (on a natural logarithmic scale) versus  $1/T$  from both computations and from experimental measurements.<sup>16</sup> As can be seen, NNIP predictions are generally consistent with AIMD results, demonstrating ionic self-diffusion coefficients on the order of  $10^{-5}$  to  $10^{-4}$   $\text{cm}^2/\text{s}$ . Such predictions are on the same order of magnitude with experimental measurements.<sup>16</sup> Furthermore, from the Arrhenius plots in Figure 6, both computational and experimental measurements show similar slopes and thus similar activation energies of self-diffusion. It is also interesting to note that both our computations and experimental measurement consistently show a smaller diffusion coefficient of  $\text{Cl}^-$  ions as compared to  $\text{Na}^+$  ions. We note that, despite the overall agreement (order of magnitude, slopes, and relative magnitudes between  $\text{Na}^+$  and  $\text{Cl}^-$ ) with experimental measurements,<sup>16</sup> our NNIP-MD (or AIMD) predictions slightly underestimate

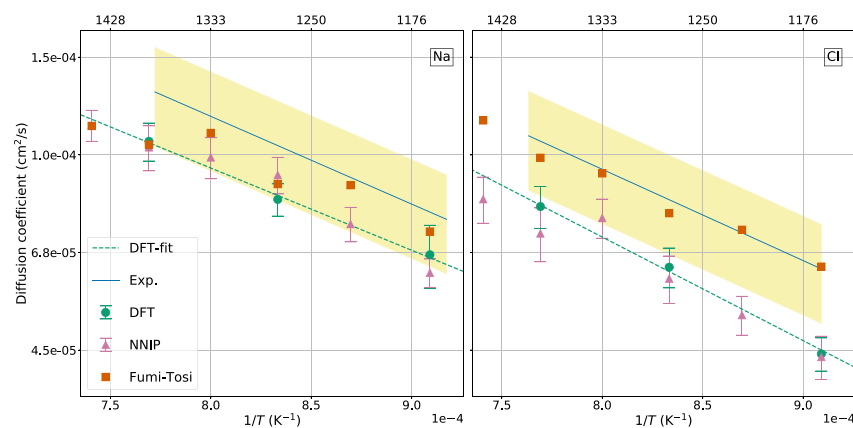


**Figure 6. Self-diffusion coefficients of molten NaCl**

Diffusion coefficients are plotted on a logarithmic scale. The temperatures corresponding to the horizontal axis are labeled on the top. Error bars on calculated values represent standard deviations. The shaded band indicates the uncertainties of experimental measurement.<sup>16</sup> For clarity, error bars associated with the predictions from the Fumi-Tosi potential<sup>29</sup> are not shown.

the diffusion coefficients. Such a tendency is in line with the slight overestimation of mass density as discussed above, indicating the effects of dispersion corrections on the bonding strength. Although the Fumi-Tosi potential<sup>29</sup> shows similar prediction errors in Na<sup>+</sup> diffusion coefficients (especially at the high temperature end), the prediction errors in Cl<sup>-</sup> diffusion coefficients are smaller. Self-diffusion coefficients can also be converted into viscosity via relations such as Stokes-Einstein equation, offering important guidelines in designing MSR with appropriate salt hydrodynamic properties.

### NNIP predictions on thermal conductivity

Thermal conductivity was calculated using the reverse non-equilibrium MD (reverse NEMD) method by Muller-Plathe.<sup>47</sup> Unlike the usual NEMD approach to calculate thermal conductivity, which imposes a temperature gradient on the system and observes the resultant heat flux, reverse NEMD imposes heat flux and measures the temperature gradient as the system's response. Specifically, in the reverse NEMD algorithm, a temperature gradient is induced by periodically exchanging kinetic energy between two atoms in two different regions. For example, if a periodic simulation box is divided into  $N$  bins ( $N$  is an even number) along dimension  $z$ , then the atom with the highest kinetic energy in the 1<sup>st</sup> bin and the atom with the lowest kinetic energy in the  $(N/2+1)$ <sup>th</sup> bin are identified to exchange kinetic energy every certain number of steps (kinetic energy should be conserved in cases of different atomic masses). This eventually establishes two symmetric temperature gradients  $dT/dz$  (see Figure 7A for examples). Because heat flux can be accurately calculated based on the exchanged kinetic energies, thermal conductivity is then calculated following

$$\lambda = -\frac{Q}{2t l_x l_y dT/dz}, \quad (\text{Equation 8})$$

where  $Q$  is the total kinetic energy exchanged during a time period of  $t$ ,  $l_x l_y$  is the cross-sectional area perpendicular to  $z$  dimension, and the factor 2 is to account for the periodicity of the simulation box. Reverse NEMD generally leads to better convergence performance than the conventional NEMD approach. Following such a reverse NEMD approach, we carried out NNIP-MD simulations under the NVE

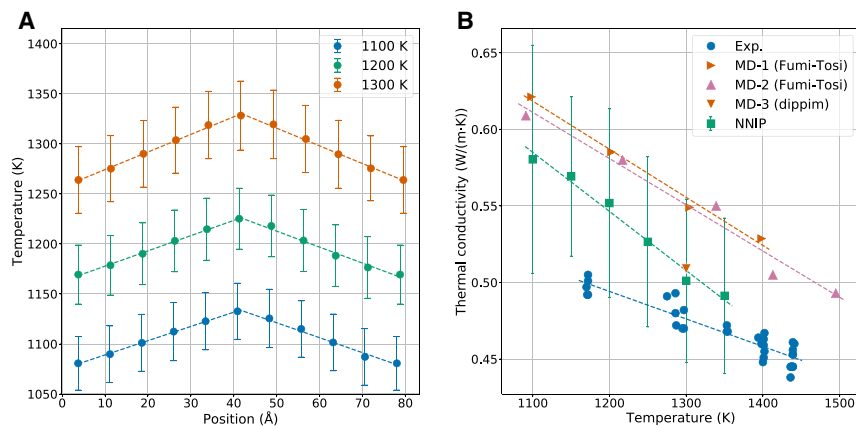


**Figure 7. Thermal conductivity of molten NaCl**

(A) Three examples of temperature profiles along the z dimension of the simulation box. Error bars represent standard deviations.

(B) Comparison of thermal conductivity between our NNIP predictions, experimental measurements,<sup>48</sup> and MD simulations using other empirical potentials (MD-1 Fumi-Tosi,<sup>49</sup> MD-2 Fumi-Tosi,<sup>50</sup> and MD-3 dipole polarizable potential<sup>51</sup>). Error bars represent standard deviations.

ensemble with equilibrium volumes over the temperature range from 1,100 K to 1,350 K. At each temperature, 10 independent simulations were carried out to obtain the average thermal conductivity. The supercell contains 3,456 atoms (the width/length ratios vary from 3.7 nm/7.4 nm to 3.8 nm/7.6 nm due to thermal expansion). All simulations were carried out over sufficient time (300 ps) to establish a converged temperature gradient. Figure 7A shows three examples of the temperature profiles established at 1,100 K, 1,200 K, and 1,300 K, respectively. As can be seen, under the imposed heat flux, all systems exhibit a linear temperature profile; thus,  $dT/dz$  can be determined by fitting to such a temperature profile. Figure 7B compares our NNIP predictions with experimental measurements,<sup>48</sup> as well as other classical MD simulation results based on the Fumi-Tosi<sup>49,50</sup> potential and dipole polarizable potential.<sup>51</sup> The NNIP predictions largely lie between the experimental measurements and Fumi-Tosi predictions, suggesting considerable improvements over this widely used empirical potential. We also note that the dipole polarizable potential<sup>51</sup> makes an excellent prediction at the single temperature point of 1,300 K, largely consistent with our NNIP prediction. Such improved prediction can be attributed to the extended representability of the polarizable potential form as well as the *ab initio* force-matching fitting procedure using proper configurations. Both aspects can now be systematically handled with artificial NNs, as demonstrated by our NNIP.

### NNIP predictions on melting/freezing point

Last, but not least, we evaluate the melting/freezing point of our NNIP model. Due to safety and efficiency considerations in MSR design, the melting/freezing point has been identified as the most important thermophysical property in choosing candidate salt systems.<sup>52</sup> Therefore, it is crucial for an interatomic potential model to capture the correct melting/freezing phase transition. We determined the melting/freezing point through a series of NVE MD simulations on coexisting crystal-liquid phases.<sup>53-55</sup> Specifically, initial (100) crystal-liquid interfaces were constructed by filling half of the periodic supercell with crystalline NaCl molecules (based on the equilibrium lattice constant at the corresponding temperature) and the other half with liquid NaCl molecules (based on the equilibrium density at the corresponding

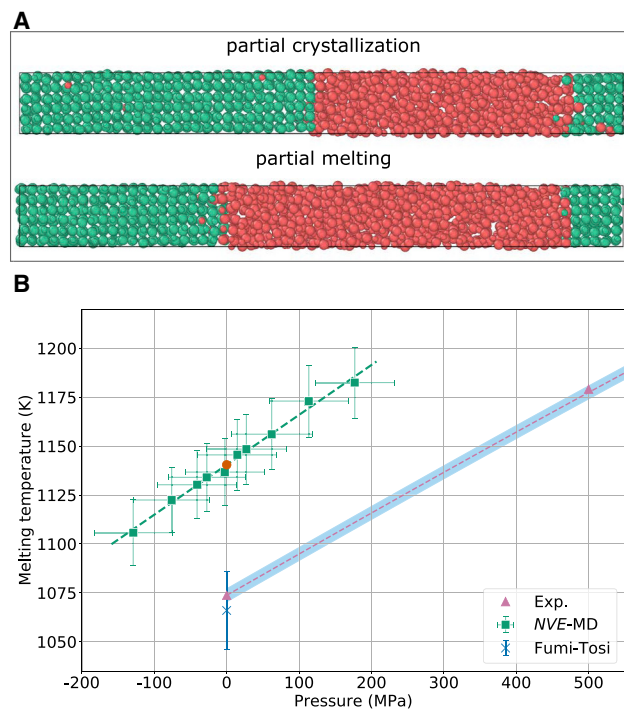


**Figure 8. Melting/freezing temperature of NaCl**

(A) Two examples of coexisting phases. Liquid (also point defects in crystalline NaCl) and crystal phases are colored in red and green, respectively. (B) Melting temperature versus pressure. The zero-pressure melting temperature (red dot marker) is determined as 1,140 K, which is 66 K higher than that of experimental measurement (1,074 K).<sup>56</sup> Melting/freezing point predicted from the Fumi-Tosi potential is from Zykova-Timan et al.<sup>55</sup> Error bars represent the standard deviations of calculated data points, although the shaded band represents the standard deviations of experimental measurements.

temperature). The simulation box contains  $\sim 2,000$  atoms with dimensions of  $\sim 17.6 \text{ nm} \times 1.76 \text{ nm} \times 1.76 \text{ nm}$ . Then, the system was slightly equilibrated at an estimated melting temperature under  $NPT$  conditions at zero pressure. With this equilibrated configuration, internal energy variations were introduced in subsequent  $NVE$  MD simulations to probe the local crystal-liquid phase boundary (Clapeyron equation). Partial crystallization or melting occurred in these  $NVE$  MD simulations, but the systems always remained in a two-phase coexisting state for a simulated time of 2 ns. Figure 8A shows two typical examples of the two-phase coexisting system, demonstrating partial crystallization and partial melting during  $NVE$  MD simulations. Figure 8B plots the observed melting temperature versus observed pressure. As can be seen from the linear fitting of this local phase boundary, the estimated melting/freezing point at zero pressure is 1,140 K, which is 66 K higher than that from experimental measurement (1,074 K).<sup>56</sup> This difference between our NNIP prediction and the experimental result is within a reasonable agreement, especially when considering that AIMD simulations included dispersion corrections on crystalline structures such that an increased crystal bonding (also see Table 1) and thus higher melting point is expected (compared to AIMD simulations without dispersion corrections). The Fumi-Tosi potential<sup>29</sup> was fitted to experimental crystal properties; thus, it shows a closer prediction<sup>55</sup> to the experimental measurements. We emphasize that performing melting point predictions with this technique would have been prohibitively expensive with AIMD due to size ( $\mathcal{O}(1000)$  atoms) and simulation time (ns) requirements. As such, NNIPs can also be seen as an approach to extrapolate the

**Table 1. Comparisons of various crystalline phase properties**

	DFT-D2	Exp.	NNIP	DFT	DFT-spin
$a_0$ (Å)	5.657	5.64 <sup>a</sup>	5.658	5.693	5.691
$E_{\text{coh}}$ (eV/ Na-Cl pair)	7.19	6.62 <sup>b,c</sup>	7.07	6.71	6.29
$C_{11}$ (GPa)	82.4	49.47 <sup>d</sup>	78.2	46.8	50.5
$C_{12}$ (GPa)	13.4	12.88 <sup>d</sup>	10.9	10.1	10.7
$C_{44}$ (GPa)	13.1	12.87 <sup>d</sup>	11.1	11.5	10.2
$\gamma_{(100)}$ (meV / Å <sup>2</sup> )	17.4	–	16.6	–	–
$\gamma_{(110)}$ (meV / Å <sup>2</sup> )	29.1	–	27.9	–	–
$\gamma_{(111)\text{-Cl}}$ (meV / Å <sup>2</sup> )	43.4	–	25.2	–	–
$\gamma_{(111)\text{-Na}}$ (meV / Å <sup>2</sup> )	27.6	–	20.0	–	–
$E_{\text{f}}^{\text{Schottky,1NN}}$ (eV)	1.68	–	1.49	–	–
$E_{\text{f}}^{\text{Schottky,2NN}}$ (eV)	2.14	–	1.90	–	–
$E_{\text{f}}^{\text{Schottky,3NN}}$ (eV)	2.18	–	1.97	–	–
$E_{\text{f}}^{\text{Schottky,4NN}}$ (eV)	2.31	–	2.10	–	–
$E_{\text{f}}^{\text{Schottky,5NN}}$ (eV)	2.34	–	2.13	–	–
$E_{\text{coh}}^{\text{CsCl}}$ (eV/ Na-Cl pair)	7.01	–	6.97	–	–
$E_{\text{coh}}^{\text{Zincblende}}$ (eV/ Na-Cl pair)	6.84	–	6.82	–	–

<sup>a</sup>Barrett and Wallace<sup>57</sup> measured at room temperature

<sup>b</sup>Chase<sup>46</sup>

<sup>c</sup>Li et al.<sup>58</sup>

<sup>d</sup>Lide et al.<sup>59</sup> measured at room temperature

AIMD predictions to relevant scales for applications, and they can be used to compare and rank different underlying theoretical approximations (such as exchange and correlation functional) according to novel experimental benchmarks.

Through these extensive validations, we see that our NNIP not only accurately reproduces AIMD results but also agrees well with experimental measurements; therefore, we conclude that this NNIP is capable of predicting the structural, thermophysical, and transport properties of molten NaCl in relevant temperature ranges.

### NNIP predictions on crystalline-phase properties

To further show the robustness of the NNIP, we now validate common properties of the B1 phase NaCl. Figure 9A shows the 0 K equation of state for B1 phase over lattice constants strained from  $-11.6\%$  to  $+17.0\%$ . Overall, NNIP predictions are in excellent agreement with DFT calculations except that deviations appear to be increasing when the potential energy is above roughly  $-3.3$  eV/atom. A similar phenomenon has also been observed in Figure 1A, where the testing errors become more scattered with increasing potential energy. This is a typical issue due to uneven/insufficient sampling of those high-energy configurations in the training dataset. If high-energy configurations are important in practical applications, one may simply increase the proportion of these configurations in the training dataset, adopt proper weighting strategy on training dataset,<sup>60</sup> or even take the advantage of well-established empirical potentials.<sup>61</sup> The derived bulk modulus from fitting to the Birch-Murnaghan equation of state are 29.6 GPa and 31.7 GPa for DFT and NNIP, respectively. Once again, our NNIP prediction agrees well with DFT calculations; however, the DFT prediction itself is  $\sim 25\%$  higher than the experimentally derived bulk modulus at zero pressure (24.0 GPa).<sup>62</sup> Such a difference may be due to the addition of van der Waals corrections in our DFT calculation, which leads to a much higher  $C_{11}$  value than that without dispersion correction (see Table 1 for details). Figure 9B shows the diatomic interactions as a function of the interatomic distance: Na-Na interactions and Cl-Cl interactions show excellent agreement with DFT

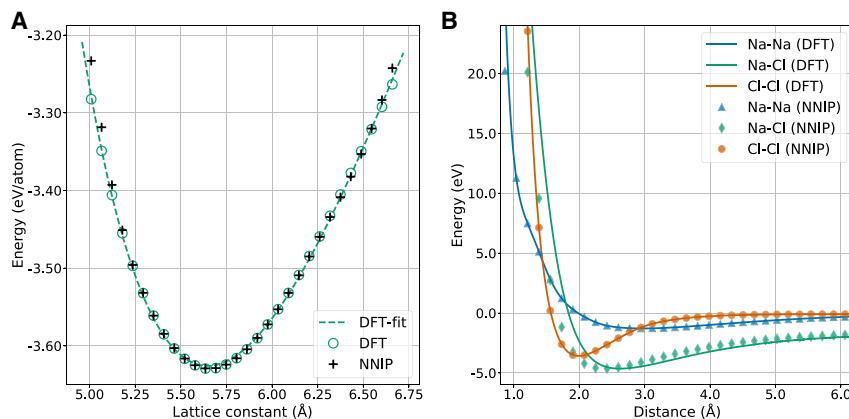


**Figure 9. Potential energy as a function of interatomic distance**

(A) Equation of state for the B1 phase NaCl at zero temperature.  
(B) Diatomic interactions.

results up to the potential energy level of  $\sim 25.0$  eV, although Na-Cl interactions show relatively larger deviations below the equilibrium distance. Such deviations in Na-Cl interactions also suggest an insufficient sampling of the Na-Cl dimer configurations when considering many other Na-Cl pairs embedded in the ionic liquid. Nevertheless, these diatomic interactions are sufficient to provide short-range repulsive interactions, especially when temperatures are well above the melting point.

Table 1 shows more comparisons of various B1 phase properties as predicted by NNIP and DFT simulations and as measured experimentally. We also include results from DFT calculations without van der Waals corrections (denoted as DFT) and spin-polarized DFT calculations (no dispersion corrections, denoted as DFT-spin) for comparison. All DFT-predicted lattice constants are slightly larger than the experimental measurement,<sup>57</sup> even though the latter was measured at room temperature. Among DFT predictions, those without dispersion corrections generally lead to slightly larger lattice constants. Our NNIP predicts a lattice constant nearly the same as the reference DFT calculation, DFT-D2. The cohesive energy  $E_{\text{coh}}$  of the B1 phase was calculated as

$$E_{\text{coh}} = nE_{\text{Na}} + nE_{\text{Cl}} - nE_{\text{NaCl}}, \quad (\text{Equation 9})$$

where  $n$  is the number of Na-Cl pairs and  $E_{\text{Na}}$ ,  $E_{\text{Cl}}$ , and  $E_{\text{NaCl}}$  are the energies of an isolated Na atom, isolated Cl atom, and the bulk B1 phase, respectively. DFT predictions for the cohesive energy decrease going from DFT-D2, DFT, to DFT-spin. This is because dispersion corrections increase bonding in the bulk phase although spin-polarization lowers the energy of isolated atoms with negligible effects on the energetics of the bulk phase. The experimental value<sup>46,58</sup> is close to DFT results without both the vdW correction and spin polarization, possibly due to the cancellation of errors. As expected, our NNIP prediction agrees well with that of dispersion-corrected DFT results. Elastic constants were calculated using the finite deformation method. As can be seen in Table 1, our NNIP predictions are consistent with DFT-D2 results. As adding dispersion corrections leads to stronger bonding in the bulk phase, DFT-D2 predictions are  $\sim 70\%$ ,  $\sim 30\%$ , and  $\sim 20\%$  higher in  $C_{11}$ ,  $C_{12}$ , and  $C_{44}$ , respectively, in comparison to those without dispersion corrections. As for the comparison with experimental measurements<sup>59</sup> available at room temperature, all DFT calculations need to be improved for better agreement.

### Transferability of NNIP

Transferability is an important aspect in the development and application of an interatomic potential. In the following, we demonstrate that our NNIP shows good transferability to a wide range of unseen configurations. First of all, we compare the NNIP energies of randomly picked configurations from high-temperature, high-pressure liquids (2,000 K+2 GPa and 3,000 K+5 GPa), which were not considered in our training data, to corresponding DFT energies. As can be seen in [Figure S7](#), the mean absolute errors are generally less than 3 meV/atom, suggesting excellent transferability to unseen liquid conditions. Second, we calculate the cohesive energies of CsCl and zincblende structures using our NNIP and compared them to DFT results (see [Table 1](#)). Again, the comparisons show excellent agreement, suggesting robustness in describing unseen crystalline structures. Third, we further test our NNIP's transferability on the Schottky defect formation energies. As shown in [Table 1](#), in comparison with DFT calculations, our NNIP prediction correctly captures the trend of formation energy change with respect to  $V_{\text{Na}}-V_{\text{Cl}}$  separation (up to 5<sup>th</sup> nearest neighbor distance), with prediction errors  $\leq 10\%$ . Finally, we test our NNIP with surface energies. To this end, we used slab configurations with a vacuum thickness of 24 Å separating periodic images. Surface energies are calculated according to

$$\gamma = \frac{1}{2A} \left[ E_n - \frac{N_n(E_n - E_{n-1})}{(N_n - N_{n-1})} \right], \quad (\text{Equation 10})$$

where  $n = 12$  is the number of layers,  $E_n$  is the potential energy of the slab with  $n$  layers,  $E_{n-1}$  is the potential energy of the slab with  $n-1$  layers,  $N_n$  is the number of atoms in the slab with  $n$  layers,  $N_{n-1}$  is the number of atoms in the slab with  $n-1$  layers, and  $A$  is the surface area. The second term in the bracket of [Equation 11](#) represents the corresponding bulk energy. A flat surface was considered for both (100) and (110) surfaces. The (111) surface may terminate with either Cl species or Na species, and we adopted the octopolar reconstructions<sup>63</sup> to eliminate the long-range dipole interactions and maintain charge neutrality (see [Figure S8](#) for the atomistic configurations of these surface structures). As can be seen in [Table 1](#), our NNIP predictions on both (100) and (110) surface energies only differ by  $\sim 1.0 \text{ meV}/\text{\AA}^2$  (or  $\sim 16 \text{ mJ}/\text{m}^2$ ) from DFT calculations, although the predictions on (111)-Cl and (111)-Na surface energies differ by  $18.2 \text{ meV}/\text{\AA}^2$  (or  $291 \text{ mJ}/\text{m}^2$ ) and  $7.6 \text{ meV}/\text{\AA}^2$  (or  $122 \text{ mJ}/\text{m}^2$ ), respectively. This difference in NNIP prediction error can be understood by considering that both (100) and (110) surfaces have local atomic neighborhoods with a 1:1 Na/Cl ratio but less neighboring atoms; thus, the local atomic environment still shares certain similarities with configurations in our training dataset. In contrast, for an octopolar (111) surface, the flat termination is reconstructed such that the outermost layer only contains 1/4 of the full lattice sites, although the two layers below contain 3/4 and 4/4 of the full lattice sites, respectively. Compared to both liquid and B1 structures, atoms on the octopolar (111) surface show quite different local atomic environments in terms of coordination number and species involved. Therefore, through these extensive property validations on liquid and crystalline phases, we have tested the limits of our NNIP for both interpolation within the configuration space close to the training set and for extrapolation out of it. Given the excellent transferability for a wide range of configurations of interest, we believe this NNIP is highly capable of simulating molten NaCl as well as the crystalline phase.

### DISCUSSION

To recap, we have applied the Behler-Parrinello NN framework<sup>34</sup> to develop a robust interatomic potential for a prototype NaCl molten salt system. Through

proper design of the training dataset and minimizing a loss function considering both potential energy and atomic forces, our NNIP achieves a DFT-level accuracy in energy/force predictions and offers excellent stability of MD simulations under various ensembles. Meanwhile, its computational cost is at least three orders of magnitude lower than AIMD and only one order of magnitude higher than the Fumi-Tosi potential (see [Figure S9](#)). Extensive material property validations, including the structural/thermophysical/transport properties of molten NaCl and crystalline phase properties, demonstrate remarkable and consistent agreement between NNIP-MD and AIMD simulations. Furthermore, these NNIP-MD-based property evaluations also agree well with a wide range of experimental measurements, demonstrating the potential of NNIP for robust molten salt modeling. We emphasize that a medium-range truncated NN, even without any explicit charge learning, appears sufficient to capture the effects of long-range electrostatic interactions in molten salts. This is both due to sufficient screening of the electrostatic potential thanks to the molten salt medium and because NNIP is trained with energies and forces obtained from AIMD calculations that consistently include the long-range interactions. However, if accurate energetics is crucial, explicit treatment of the Coulomb interaction may be needed for ions with a separation larger than the cutoff distance and in a lesser electrostatically screened medium than the molten salt. On the opposite end, our NN learning strategy also stressed the sub-nearest-neighbor interactions, as atoms in the liquid phase may gain enough kinetic energy to enter such non-equilibrium ranges.

Regarding practical applications, several challenges remain to be addressed by further work. First, real-world molten salt systems are often mixtures of two or more salts and also involve various impurities, such as fission/corrosion products. Thus, multi-element interatomic potentials that are capable of handling extra chemical complexities<sup>64,65</sup> are highly desired. Second, a high-quality training dataset requires careful validations of *ab initio* calculations with existing experimental results as well as minimized convergence errors among different systems. Third, efficient and adaptive sampling of training data (such as active learning) and deep learning on local atomic environment descriptors<sup>66</sup> should be explored to reduce human bias and effort. Despite these challenges, NNIP-MD-based modeling represents a promising pathway to mitigate the long-standing accuracy-versus-cost trade-off in molten salt assessments. Particularly, unlike most empirical potentials, which are designed for specific applications, the predictive power of NNIP can be systematically improved by augmenting the training dataset to include various phases, defects, unstable states, chemical species, and so forth, thus enabling simulations to approach one step closer to complex, real-world applications.

## EXPERIMENTAL PROCEDURES

### Resource availability

#### Lead contact

Further information and requests for resources should be directed to and will be fulfilled by the lead contact, J. Li ([liju@mit.edu](mailto:liju@mit.edu)).

#### Materials availability

This study did not generate any new reagents.

#### Data and code availability

The authors declare that the data supporting the findings of this study are available within the article and the [Supplemental information](#). All other data and codes are available from the lead contact upon reasonable request.

### Local atomic environment descriptors

In this work, we have used 30 equidistant Gaussian centers for the radial part and 6 equidistant Gaussians with 6 equally spaced  $\theta_s$  centers for the angular part of the descriptor. Considering the species resolution, we have used 60 radial (30 Na-Na + 30 Na-Cl) and 108 angular components ( $6 \times 6$  Na-Na-Na +  $6 \times 6$  Na-Na-Cl +  $6 \times 6$  Cl<sup>-</sup>-Na-Cl) or a vector of dimension 168 that describes the local atomic environment of each atom (see Table S2 for the values of other parameters used). Also see Note S1 and Figure S10 for more discussions. We note that descriptor function choice is not unique; other definitions<sup>67,68</sup> are equally valid as long as the local atomic environment is described accurately.

### Ab initio quantum mechanical calculations

All configurations in our training/testing/validation dataset were generated using the Vienna *Ab initio* simulation package (VASP).<sup>69-72</sup> In our *ab initio* calculations, generalized gradient approximation (GGA) in the form of Perdew-Burke-Ernzerhof (PBE)<sup>73</sup> was adopted for the exchange-correlation functional. Core electrons are modeled by projector-augmented wave (PAW) pseudo-potentials<sup>74,75</sup> (Na\_pv: 2p62 s1, Cl: 3 s<sup>2</sup>3p5) with an energy cutoff of 600 eV. Brillouin zone integration was performed using the  $\Gamma$  point only. Gaussian smearing with a width of 0.05 eV was used for the partial occupancies of states. Based on a previous study,<sup>43</sup> van der Waals corrections with the DFT-D2 scheme of Grimme<sup>76</sup> were added to DFT energy. The convergence criterion for electronic self-consistent calculations is 0.1 meV. AIMD simulations were carried out under either the NVT (Nose-Hoover thermostat) or the NPT (Langevin thermostat) ensemble with a timescale of  $10^1$ – $10^2$  ps at a time step of 1–3 fs. Configurations were extracted every  $\sim 30$  fs. A 64-atom supercell was used for molten NaCl AIMD (the non-1:1 Na/Cl ratio supercells generally have less than 64 atoms), although a relatively larger supercell size (216 atoms) was used for crystalline NaCl calculations. We note that cell-size effects could be significant for dynamical properties from AIMD simulations; however, small supercells are acceptable for NN training, as the training process only considers the total energy and atomic forces from different configurations.

### NN training

NN training consists of searching for a set of optimal model parameters (weights and biases) that minimizes a predefined cost function, typically finding a local minimum rather than the global minimum value. Here, we use a quadratic loss on total energies and atomic forces as well as an L1 norm regularization,

$$C_b = \sum_{i \in \text{batch}} \left[ (E_i^{\text{DFT}} - E_i^{\text{NN}})^2 + c_f \sum_{j=1}^{N_{\text{at}}} (F_{ij}^{\text{DFT}} - F_{ij}^{\text{NN}})^2 \right] + c_1 \|W\|_1, \quad (\text{Equation 11})$$

where the subscript  $b$  in  $C_b$  indicates that the cost function is defined over a mini-batch (stochastic gradient descent method),  $N_{\text{at}}$  is the total number of atoms in the system,  $E_i^{\text{DFT}}$  is the target energy (from the DFT calculation) of configuration  $i$ ,  $E_i^{\text{NN}}$  is the corresponding NN energy prediction,  $F_{ij}^{\text{DFT}}$  is the target force (from the DFT calculation) of atom  $j$  in configuration  $i$ ,  $F_{ij}^{\text{NN}}$  is the corresponding NN force prediction computed analytically through the chain rule,  $\|W\|_1$  is the L1 norm regularization term that helps reduce redundant weight parameters to prevent overfitting, and  $c_f$  and  $c_1$  are parameters to tune the weight of force-based loss and L1-regularization-based loss, respectively.  $c_f = 0.1$  and  $c_1 = 0.01$  were adopted in this work. L1 regularization was adopted in particular with the earlier cycles of the training dataset in mind, when the network size ( $\sim 15\text{k}$  parameters) was comparable to the training

dataset size. All our training was carried out using the PANNA package,<sup>42</sup> which also provides an implementation of a new “pair\_style panna” in LAMMPS<sup>77</sup> for NNIP-based MD simulations. Performance tests using a local computing cluster (64 cores as in 2 nodes, each with 2 × 16 cores of Intel Xeon 2.1 GHz and 128 GB RAM) on a range of cell sizes (from 64 atoms to 1,024 atoms) show that the cost, in terms of CPU (central processing unit) hours per atom per MD step, for the chosen NNIP architecture and for Fumi-Tosi empirical potential<sup>29</sup> are on the order of 10<sup>-6</sup> and 10<sup>-7</sup>, respectively, making NNIP only one order of magnitude more costly than the Fumi-Tosi potential (see Figure S9).<sup>29</sup>

### SUPPLEMENTAL INFORMATION

Supplemental information can be found online at <https://doi.org/10.1016/j.xcrp.2021.100359>.

### ACKNOWLEDGMENTS

This material is based upon work supported by the Department of Energy under award number DE-NE0008751. J.L. also acknowledges support by the Office of Naval Research Multidisciplinary University Research Initiative Award no. ONR N00014-18-1-2497. The work of E. Küçükbenli and E. Kaxiras was supported by a DOE grant, BES Award DE-SC0019300. This work used the high-performance computing resources provided by MIT Engaging cluster and FASRC Cannon cluster supported by the FAS Division of Science Research Computing Group at Harvard University. This work also used the Extreme Science and Engineering Discovery Environment (XSEDE) resources at the Texas Advanced Computing Center (TACC) through allocation DMR190055 and DMR200010. Disclaimer: “This report was prepared as an account of work sponsored by an agency of the United States Government. Neither the United States Government nor any agency thereof, nor any of their employees, makes any warranty, express or implied, or assumes any legal liability or responsibility for the accuracy, completeness, or usefulness of any information, apparatus, product, or process disclosed, or represents that its use would not infringe privately owned rights. Reference herein to any specific commercial product, process, or service by trade name, trademark, manufacturer, or otherwise does not necessarily constitute or imply its endorsement, recommendation, or favoring by the United States Government or any agency thereof. The views and opinions of authors expressed herein do not necessarily state or reflect those of the United States Government or any agency thereof.”

### AUTHOR CONTRIBUTIONS

Q.-J.L., E. Küçükbenli, B.K., E. Kaxiras, and J.L. designed the project. Q.-J.L. and E. Küçükbenli carried out the machine learning design and calculations. Q.-J.L. and S.L. performed the high-throughput DFT calculations. Q.-J.L. and E. Küçükbenli led the writing of the manuscript. All authors contributed to the data analysis and discussions.

### DECLARATION OF INTERESTS

The authors declare no competing interests.

Received: December 9, 2020

Revised: January 26, 2021

Accepted: February 9, 2021

Published: March 2, 2021

## REFERENCES

1. Le Brun, C. (2007). Molten salts and nuclear energy production. *J. Nucl. Mater.* 360, 1–5.
2. Williams, D.F., and Clarno, K.T. (2008). Evaluation of salt coolants for reactor applications. *Nucl. Technol.* 163, 330–343.
3. Serp, J., Allibert, M., Beneš, O., Delpech, S., Feynberg, O., Ghetta, V., Heuer, D., Holcomb, D., Ignatiev, V., Kloosterman, J.L., et al. (2014). The molten salt reactor (MSR) in generation IV: overview and perspectives. *Prog. Nucl. Energy* 77, 308–319.
4. Zhang, H.L., Baeyens, J., Degreè, J., and Cacères, G. (2013). Concentrated solar power plants: review and design methodology. *Renew. Sustain. Energy Rev.* 22, 466–481.
5. Pelay, U., Luo, L., Fan, Y., Stitou, D., and Rood, M. (2017). Thermal energy storage systems for concentrated solar power plants. *Renew. Sustain. Energy Rev.* 79, 82–100.
6. Grimes, W.R. (1970). Molten-salt reactor chemistry. *Nucl. Appl. Technol.* 8, 137–155.
7. Zhang, J. (2019). Impurities in primary coolant salt of FHRs: chemistry, impact, and removal methods. *Energy Technol. (Weinheim)* 7, 1900016.
8. Guo, S., Zhang, J., Wu, W., and Zhou, W. (2018). Corrosion in the molten fluoride and chloride salts and materials development for nuclear applications. *Prog. Mater. Sci.* 97, 448–487.
9. Frazier, P.I., and Wang, J. (2016). Bayesian optimization for materials design. In *Information Science for Materials Discovery and Design Springer Series in Materials Science*, T. Lookman, F.J. Alexander, and K. Rajan, eds. (Springer International Publishing), pp. 45–75.
10. Lookman, T., Balachandran, P.V., Xue, D., and Yuan, R. (2019). Active learning in materials science with emphasis on adaptive sampling using uncertainties for targeted design. *npj Comput. Mater.* 5, 21.
11. Cantor, S., Cooke, J.W., Dworkin, A.S., Robbins, G.D., Thoma, R.E., and Watson, G.M. (1968). *Physical Properties of Molten-Salt Reactor Fuel, Coolant, and Flush Salts* (Oak Ridge National Lab).
12. Bamberger, C.E. (1975). Experimental techniques in molten fluoride chemistry. In *Advances in Molten Salt Chemistry, Volume 3*, J. Braunstein, G. Mamantov, and G.P. Smith, eds. *Advances in Molten Salt Chemistry* (Springer US), pp. 177–248.
13. Thoma, R.E. (1975). Phase diagrams of binary and ternary fluoride systems. In *Advances in Molten Salt Chemistry, Volume 3*, J. Braunstein, G. Mamantov, and G.P. Smith, eds. *Advances in Molten Salt Chemistry* (Springer US), pp. 275–455.
14. Edwards, F.G., Enderby, J.E., Howe, R.A., and Page, D.I. (1975). The structure of molten sodium chloride. *J. Phys. C Solid State Phys.* 8, 3483–3490.
15. Biggin, S., and Enderby, J.E. (1982). Comments on the structure of molten salts. *J. Phys. C Solid State Phys.* 15, L305–L309.
16. Janz, G.J., and Bansal, N.P. (1982). Molten salts data: diffusion coefficients in single and multi-component salt systems. *J. Phys. Chem. Ref. Data* 11, 505–693.
17. Di Cicco, A., Minicucci, M., and Filipponi, A. (1997). New advances in the study of local structure of molten binary salts. *Phys. Rev. Lett.* 78, 460–463.
18. Hohenberg, P., and Kohn, W. (1964). Inhomogeneous electron gas. *Phys. Rev.* 136, B864–B871.
19. Kohn, W., and Sham, L.J. (1965). Self-consistent equations including exchange and correlation effects. *Phys. Rev.* 140, A1133–A1138.
20. Bengtson, A., Nam, H.O., Saha, S., Sakidja, R., and Morgan, D. (2014). First-principles molecular dynamics modeling of the LiCl–KCl molten salt system. *Comput. Mater. Sci.* 83, 362–370.
21. Nam, H.O., and Morgan, D. (2015). Redox condition in molten salts and solute behavior: a first-principles molecular dynamics study. *J. Nucl. Mater.* 465, 224–235.
22. Li, X., Song, J., Shi, S., Yan, L., Zhang, Z., Jiang, T., and Peng, S. (2017). Dynamic fluctuation of  $U^{3+}$  coordination structure in the molten LiCl–KCl eutectic via first principles molecular dynamics simulations. *J. Phys. Chem. A* 121, 571–578.
23. Nam, H.O., Bengtson, A., Vörtler, K., Saha, S., Sakidja, R., and Morgan, D. (2014). First-principles molecular dynamics modeling of the molten fluoride salt with Cr solute. *J. Nucl. Mater.* 449, 148–157.
24. Lv, X., Han, Z., Chen, J., Jiang, L., Xu, Z., and Liu, Q. (2018). First-principles molecular dynamics study of ionic structure and transport properties of LiF–NaF–AlF<sub>3</sub> molten salt. *Chem. Phys. Lett.* 706, 237–242.
25. Guo, H., Li, J., Zhang, H., Li, T., Luo, J., Yu, X., Wu, S., and Zong, C. (2019). First-principles molecular dynamics investigation on KF–NaF–AlF<sub>3</sub> molten salt system. *Chem. Phys. Lett.* 730, 587–593.
26. Li, B., Dai, S., and Jiang, D. (2019). First-principles molecular dynamics simulations of UCl<sub>n</sub>–NaCl ( $n = 3, 4$ ) molten salts. *ACS Appl. Energy Mater.* 2, 2122–2128.
27. Klix, A., Suzuki, A., and Terai, T. (2006). Study of tritium migration in liquid Li<sub>2</sub>BeF<sub>4</sub> with ab initio molecular dynamics. *Fusion Eng. Des.* 81, 713–717.
28. Wu, F., Roy, S., Ivanov, A.S., Gill, S.K., Topsakal, M., Dooryhee, E., Abeykoon, M., Kwon, G., Gallington, L.C., Halstenberg, P., et al. (2019). Elucidating ionic correlations beyond simple charge alternation in molten MgCl<sub>2</sub>–KCl mixtures. *J. Phys. Chem. Lett.* 10, 7603–7610.
29. Fumi, F.G., and Tosi, M.P. (1964). Ionic sizes and born repulsive parameters in the NaCl-type alkali halides—I: The Huggins-Mayer and Pauling forms. *J. Phys. Chem. Solids* 25, 31–43.
30. Sangster, M.J.L., and Dixon, M. (1976). Interionic potentials in alkali halides and their use in simulations of the molten salts. *Adv. Phys.* 25, 247–342.
31. Aguado, A., Bernasconi, L., Jahn, S., and Madden, P.A. (2003). Multipoles and interaction potentials in ionic materials from planewave-DFT calculations. *Faraday Discuss.* 124, 171–184, discussion 205–213, 453–455.
32. Salanne, M., Rotenberg, B., Jahn, S., Vuilleumier, R., Simon, C., and Madden, P.A. (2012). Including many-body effects in models for ionic liquids. *Theor. Chem. Acc.* 131, 1143.
33. Salanne, M., and Madden, P.A. (2011). Polarization effects in ionic solids and melts. *Mol. Phys.* 109, 2299–2315.
34. Behler, J., and Parrinello, M. (2007). Generalized neural-network representation of high-dimensional potential-energy surfaces. *Phys. Rev. Lett.* 98, 146401.
35. Bartók, A.P., Payne, M.C., Kondor, R., and Csányi, G. (2010). Gaussian approximation potentials: the accuracy of quantum mechanics, without the electrons. *Phys. Rev. Lett.* 104, 136403.
36. Artrith, N., Morawietz, T., and Behler, J. (2011). High-dimensional neural-network potentials for multicomponent systems: applications to zinc oxide. *Phys. Rev. B* 83, 153101.
37. Smith, J.S., Isayev, O., and Roitberg, A.E. (2017). ANI-1: an extensible neural network potential with DFT accuracy at force field computational cost. *Chem. Sci. (Camb.)* 8, 3192–3203.
38. Schütt, K.T., Arbabzadah, F., Chmiela, S., Müller, K.R., and Tkatchenko, A. (2017). Quantum-chemical insights from deep tensor neural networks. *Nat. Commun.* 8, 13890.
39. Onat, B., Cubuk, E.D., Malone, B.D., and Kaxiras, E. (2018). Implanted neural network potentials: Application to Li-Si alloys. *Phys. Rev. B* 97, 094106.
40. Pun, G.P.P., Batra, R., Ramprasad, R., and Mishin, Y. (2019). Physically informed artificial neural networks for atomistic modeling of materials. *Nat. Commun.* 10, 2339.
41. Wood, M.A., and Thompson, A.P. (2018). Extending the accuracy of the SNAP interatomic potential form. *J. Chem. Phys.* 148, 241721.
42. Lot, R., Pellegrini, F., Shaidu, Y., and Küçükbenli, E. (2020). PANNA: properties from artificial neural network architectures. *Comput. Phys. Commun.* 256, 107402.
43. Liu, M., Masset, P., and Gray-Weale, A. (2014). Solubility of sodium in sodium chloride: a density functional theory molecular dynamics study. *J. Electrochem. Soc.* 161, E3042–E3048.
44. Kirshenbaum, A.D., Cahill, J.A., McGonigal, P.J., and Grosse, A.V. (1962). The density of liquid NaCl and KCl and an estimate of their critical constants together with those of the other alkali halides. *J. Inorg. Nucl. Chem.* 24, 1287–1296.
45. Janz, G.J. (1988). Thermodynamic and transport properties for molten salts: correlation equations for critically evaluated density, surface tension, electrical conductance, and viscosity data. *J. Phys. Chem. Ref. Data* 17, 1–309.

46. Chase, M.W.; National Institute of Standards and Technology (U.S.) (1998). NIST-JANAF Thermochemical Tables (American Chemical Society/American Institute of Physics for the National Institute of Standards and Technology).
47. Müller-Plathe, F. (1997). A simple nonequilibrium molecular dynamics method for calculating the thermal conductivity. *J. Chem. Phys.* *106*, 6082–6085.
48. Nagasaka, Y., Nakazawa, N., and Nagashima, A. (1992). Experimental determination of the thermal diffusivity of molten alkali halides by the forced Rayleigh scattering method. I. Molten LiCl, NaCl, KCl, RbCl, and CsCl. *Int. J. Thermophys.* *13*, 555–574.
49. Ohtori, N., Oono, T., and Takase, K. (2009). Thermal conductivity of molten alkali halides: temperature and density dependence. *J. Chem. Phys.* *130*, 044505.
50. Galamba, N., Nieto de Castro, C.A., and Ely, J.F. (2004). Thermal conductivity of molten alkali halides from equilibrium molecular dynamics simulations. *J. Chem. Phys.* *120*, 8676–8682.
51. Ohtori, N., Salanne, M., and Madden, P.A. (2009). Calculations of the thermal conductivities of ionic materials by simulation with polarizable interaction potentials. *J. Chem. Phys.* *130*, 104507.
52. Williams, D.F. (2006). Assessment of Candidate Molten Salt Coolants for the Advanced High Temperature Reactor (AHTR).
53. Morris, J.R., Wang, C.Z., Ho, K.M., and Chan, C.T. (1994). Melting line of aluminum from simulations of coexisting phases. *Phys. Rev. B Condens. Matter* *49*, 3109–3115.
54. Purja Pun, G.P., and Mishin, Y. (2009). Development of an interatomic potential for the Ni-Al system. *Philos. Mag.* *89*, 3245–3267.
55. Zykova-Timan, T., Ceresoli, D., Tartaglino, U., and Tosatti, E. (2005). Physics of solid and liquid alkali halide surfaces near the melting point. *J. Chem. Phys.* *123*, 164701.
56. Akella, J., Vaidya, S.N., and Kennedy, G.C. (1969). Melting of sodium chloride at pressures to 65 kbar. *Phys. Rev.* *185*, 1135–1140.
57. Barrett, W.T., and Wallace, W.E. (1954). Studies of NaCl-KCl solid solutions. I. Heats of formation, lattice spacings, densities, Schottky defects and mutual solubilities. *J. Am. Chem. Soc.* *76*, 366–369.
58. Li, B., Michaelides, A., and Scheffler, M. (2007). Density functional theory study of flat and stepped NaCl(001). *Phys. Rev. B* *76*, 075401.
59. Lide, D.R., Baysinger, G., Chemistry, S., Berger, L.I., Goldberg, R.N., and Kehiaian, H.V. (2005). CRC Handbook of Chemistry and Physics Internet version 2005 (CRC).
60. Jeong, W., Lee, K., Yoo, D., Lee, D., and Han, S. (2018). Toward reliable and transferable machine learning potentials: uniform training by overcoming sampling bias. *J. Phys. Chem. C* *122*, 22790–22795.
61. Byggmästar, J., Hamedani, A., Nordlund, K., and Djurabekova, F. (2019). Machine-learning interatomic potential for radiation damage and defects in tungsten. *Phys. Rev. B* *100*, 144105.
62. Thomas, L.M., and Shanker, J. (1995). Equations of state and pressure dependence of bulk modulus for NaCl crystals. *Physica Status Solidi B* *189*, 363–369.
63. Bruno, M., Aquilano, D., Pastero, L., and Prencepe, M. (2008). Structures and surface energies of (100) and octopolar (111) faces of halite (NaCl): an *ab initio* quantum-mechanical and thermodynamical study. *Cryst. Growth Des.* *8*, 2163–2170.
64. Liang, W., Lu, G., and Yu, J. (2020). Composition-dependent microstructure evolution in liquid MgCl<sub>2</sub>-KCl: A first-principles molecular dynamics study. *J. Mol. Liq.* *309*, 113131.
65. Wu, F., Sharma, S., Roy, S., Halstenberg, P., Gallington, L.C., Mahurin, S.M., Dai, S., Bryantsev, V.S., Ivanov, A.S., and Margulis, C.J. (2020). Temperature dependence of short and intermediate range order in molten MgCl<sub>2</sub> and its mixture with KCl. *J. Phys. Chem. B* *124*, 2892–2899.
66. Zhang, L., Han, J., Wang, H., Car, R., and E, W. (2018). Deep potential molecular dynamics: a scalable model with the accuracy of quantum mechanics. *Phys. Rev. Lett.* *120*, 143001.
67. Bartók, A.P., Kondor, R., and Csányi, G. (2013). On representing chemical environments. *Phys. Rev. B* *87*, 184115.
68. Kocer, E., Mason, J.K., and Erturk, H. (2020). Continuous and optimally complete description of chemical environments using Spherical Bessel descriptors. *AIP Adv.* *10*, 015021.
69. Kresse, G., and Hafner, J. (1993). *Ab initio* molecular dynamics for liquid metals. *Phys. Rev. B Condens. Matter* *47*, 558–561.
70. Kresse, G., and Hafner, J. (1994). *Ab initio* molecular-dynamics simulation of the liquid-metal-amorphous-semiconductor transition in germanium. *Phys. Rev. B Condens. Matter* *49*, 14251–14269.
71. Kresse, G., and Furthmüller, J. (1996). Efficiency of *ab-initio* total energy calculations for metals and semiconductors using a plane-wave basis set. *Comput. Mater. Sci.* *6*, 15–50.
72. Kresse, G., and Furthmüller, J. (1996). Efficient iterative schemes for *ab initio* total-energy calculations using a plane-wave basis set. *Phys. Rev. B Condens. Matter* *54*, 11169–11186.
73. Perdew, J.P., Burke, K., and Ernzerhof, M. (1996). Generalized gradient approximation made simple. *Phys. Rev. Lett.* *77*, 3865–3868.
74. Blöchl, P.E. (1994). Projector augmented-wave method. *Phys. Rev. B Condens. Matter* *50*, 17953–17979.
75. Kresse, G., and Joubert, D. (1999). From ultrasoft pseudopotentials to the projector augmented-wave method. *Phys. Rev. B* *59*, 1758–1775.
76. Grimme, S. (2006). Semiempirical GGA-type density functional constructed with a long-range dispersion correction. *J. Comput. Chem.* *27*, 1787–1799.
77. Plimpton, S. (1995). Fast parallel algorithms for short-range molecular dynamics. *J. Comput. Phys.* *117*, 1–19.